COMMUNICATION

Brittle Fracture of 2D $MoSe_2$

Yingchao Yang, Xing Li, Minru Wen, Emily Hacopian, Weibing Chen, Yongji Gong, Jing Zhang, Bo Li, Wu Zhou, Pulickel M. Ajayan, Qing Chen, Ting Zhu, and Jun Lou**

Transition metal dichalcogenides (TMDs) represent an emerging group of 2D materials with unique electronic and optical properties.[1–5] They consist of atomic layers of hexagonal lattices formed in a MX_2 type stoichiometry, where M is a transition element from groups IV, V, or VI, and X is part of the chalcogen species S, Se, or Te. Considerable research effort has been devoted to understanding the structure of atomically thin layers of TMDs, as well as exploring their applications in field-effect transistors,[6,7] photovoltaics,[8–10] photodetectors,[2,11,12] and catalysts.[13–15] As a representative of 2D semiconducting TMDs, $MoSe_2$ has potential applications in flexible electronic and optical devices. The stability and reliability of these devices depend critically on the mechanical performance of $MoSe_2$. However, the mechanical properties of $MoSe_2$ have not been measured to date. Moreover, the deformation and failure mechanisms in materials at the 2D limit are of fundamental importance, but have been little studied by experiment.

Quantitative mechanical testing of the atomically thin TMDs is extremely challenging. Currently, atomic force microscopy (AFM) and nanoindentation are usually used to measure the mechanical properties of few-layer 2D materials.[16–20] In this approach, the 2D membrane was suspended over a perforated substrate and assumed to adhere to the circumference of the hole without slippage during AFM scanning and indentation. However, the transverse, local probing by an AFM tip can result in highly non-uniform stress and strain fields in the thin layer of a 2D material, which makes it difficult to extract the intrinsic mechanical properties from experimental measurements. Nonetheless, the AFM-based mechanical testing of 2D materials started with the measurement of elastic modulus and fracture strength of graphene.[16] Recently, Bertolazzi et al. measured the in-plane effective elastic modulus and average breaking strength of monolayer MoS_2 to be 270 ± 100 and 23 GPa, respectively.[21] The factors such as indenter radius, indentation location, and residual stress in the tested 2D materials could cause uncertainties and possible errors in quantitative measurements. In contrast to the local transverse loading by AFM, we have recently developed a nanomechanical testing device that enables the uniform in-plane loading on a freestanding membrane of 2D materials. This device has been applied to measure the fracture toughness of graphene.[22] Brittle fracture was observed in the freestanding graphene films containing a pre-crack. The measured fracture toughness of graphene is 4.0 ± 0.6 MPa $m^{-1/2}$, with the equivalent energy release rate of fracture of 15.9 J m^{-2}. Here we further developed this in-plane nanomechanical testing system with an improved dry transfer approach for fragile $MoSe_2$ membranes, and then used this system to investigate the mechanical behavior of monolayer and bilayer $MoSe_2$. The brittle failure of crack initiation, propagation, and final fracture were observed in real time. We measured the elastic modulus and fracture strength of $MoSe_2$, and further studied the origin of strength variability as well as the fragility of different 2D materials.

The large-area 2D single-crystal of $MoSe_2$ was synthesized on a Si/SiO_2 wafer by the chemical vapor deposition (CVD) method. As shown in **Figure 1**a, the smooth monolayer and bilayer $MoSe_2$ can be easily distinguished by their thickness-dependent optical contrast. More optical and scanning electron microscopy (SEM) images of monolayer $MoSe_2$ can be found in the Supporting Information Sections S1 and S2. Single crystal $MoSe_2$ typically has a size between 5 and 30 μm. We performed Raman and photoluminescence (PL) analyses to determine the number of $MoSe_2$ layers (Figure 1b,c). The sharp A_{1g} peak at a lower Raman shift of 240.0 cm^{-1} originates from out-of-plane vibration, which is characteristic of monolayer $MoSe_2$. The A_{1g} Raman mode is shifted to 242.2 cm^{-1} for bilayer $MoSe_2$, which is in agreement with previous results.[5,23,24] The PL intensity and the position of PL peak have been previously used to characterize $MoSe_2$.[5,23] Figure 1c shows the characteristic PL spectra of monolayer and bilayer $MoSe_2$ at room temperature. The high-angle annular dark-field scanning transmission electron microscope (HAADF-STEM) image of monolayer $MoSe_2$ (Figure 1d) shows the alternating bright (Se_2) and dark (Mo) sites. The intensity profile for the region highlighted by the box is plotted in Figure 1e. The neighboring Mo (weak) and Se_2 (bright) sites are separated by 1.98 Å and the Mo-Mo distance is 5.49 Å. AFM was also used to study the structure and

Dr. Y. C. Yang, X. Li, E. Hacopian, W. B. Chen, Dr. Y. J. Gong, Dr. J. Zhang, Dr. B. Li, Prof. P. M. Ajayan, Prof. J. Lou
Department of Materials Science and NanoEngineering
Rice University
Houston, TX 77005, USA
E-mail: jlou@rice.edu
X. Li, Prof. Q. Chen
Key Laboratory for the Physics and Chemistry of Nanodevices and Department of Electronics
Peking University
Beijing 100871, China
M. R. Wen
Department of Physics
Tsinghua University
Beijing 100084, China
M. R. Wen, Prof. T. Zhu
Woodruff School of Mechanical Engineering
Georgia Institute of Technology
Atlanta, GA 30332, USA
E-mail: ting.zhu@me.gatech.edu
Dr. W. Zhou
Materials Science and Technology Division
Oak Ridge National Lab
Oak Ridge, TN 37831, USA

DOI: 10.1002/adma.201604201

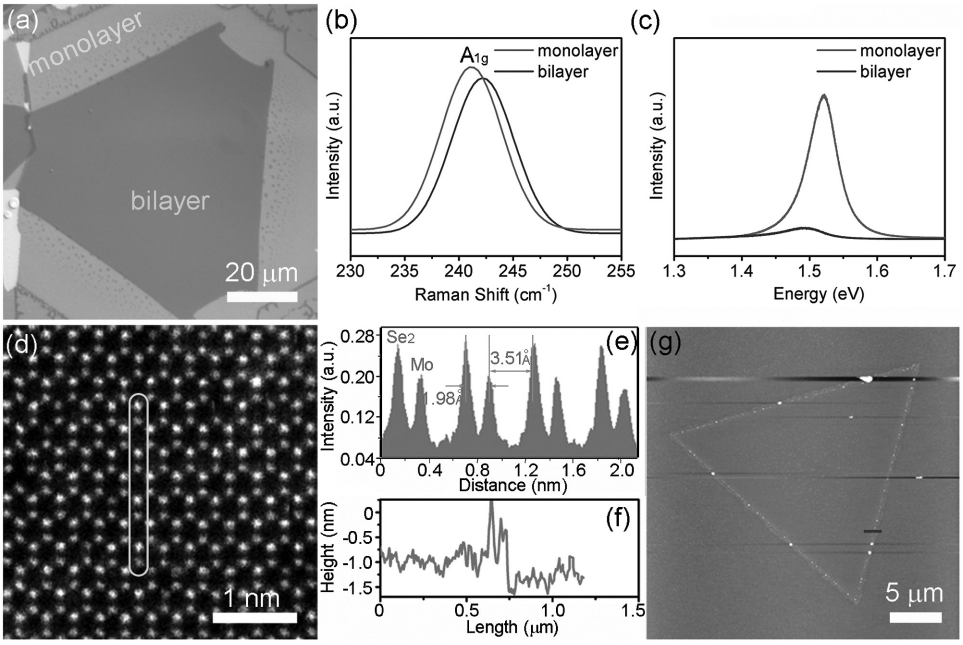

Figure 1. Morphology and structure of $MoSe_2$ grown by the CVD method. a) Optical image of monolayer/bilayer $MoSe_2$ grown on Si/SiO_2. b) Raman analysis of $MoSe_2$. c) PL analysis of $MoSe_2$. d) HAADF-STEM image of monolayer $MoSe_2$ with a perfect hexagonal lattice. e) Intensity profile for the region marked in the box in (d). The neighboring Mo (weak) and Se_2 (bright) sites are separated by 1.98 Å and the Mo-Mo distance is 5.49 Å. f) Cross-section height profile of monolayer $MoSe_2$ in (g). g) AFM image of monolayer $MoSe_2$.

geometry of $MoSe_2$. Figure 1g shows an AFM image of a monolayer $MoSe_2$ crystal, where several big particles are distributed along the triangle edges and a few small ones within the triangle domain. Such kind of particles are commonly observed in CVD-grown $MoSe_2$.[5] To determine the thickness of monolayer $MoSe_2$, we used an AFM to map out the cross-sectional height profile of $MoSe_2$ along the short line to the bottom right of Figure 1g. As shown in Figure 1f, a single step appears and the step height is ≈0.7 nm. Hence, the as-grown monolayer $MoSe_2$ has a thickness of ≈0.7 nm. The thickness analysis and AFM image of a bilayer $MoSe_2$ crystal can be found in the Supporting Information Section S3.

A critical step in the nanomechanical testing of 2D $MoSe_2$ was to transfer the atomically thin membrane of as-grown $MoSe_2$ onto a nanomechanical device. To facilitate the transfer, a thin layer of poly (methyl methacrylate) (PMMA) with thickness of 200–300 nm was coated over $MoSe_2$ grown on a Si/SiO_2 wafer. To choose a suitable transfer method, one needs to consider how to effectively remove PMMA at the end of transfer. In principle, PMMA could be removed from the PMMA/$MoSe_2$ pair by either annealing with a carrier gas of H_2 or immerging into acetone. However, the nanomechanical device that we design cannot be immerged into any liquid since the suspended shuttles can be stuck to the substrate once the nanomechanical device is taken out from the liquid. To prevent this problem, we developed a dry transfer technique to avoid the liquid damage to the suspended working layer on the testing device. The schematic of dry transfer is shown in **Figure 2**a. Specifically, the Si/SiO_2 substrate was first etched in 2.5 mol L^{-1} NaOH solution. A clean copper grid was then used to fish out PMMA/$MoSe_2$ after several washes in the DI water. The advantage of using copper grid is that the contact area between PMMA/$MoSe_2$ and the copper substrate can be reduced to prevent PMMA/$MoSe_2$ from permanently sticking to the substrate. Due to the thickness-dependent optical contrast, monolayer and bilayer $MoSe_2$ can be precisely located under an optical microscope. Figure 2b,c shows the optical images of monolayer and bilayer $MoSe_2$ crystals (covered with transparent PMMA) sitting on a copper grid. A fine tungsten probe was used to cut, pick, and load PMMA/$MoSe_2$ onto the nanomechanical device shown in Figure 2d. More optical images showing parts of the PMMA/$MoSe_2$ film after cutting can be found in the Supporting Information Section 4. The suspended $MoSe_2$ on the nanomechanical device was finally obtained after heat treatment for removing PMMA.

The 2D $MoSe_2$ crystal was cut into a rectangular shape by focus ion beam (FIB) in a dual beam SEM. **Figure 3**a shows the SEM image of a $MoSe_2$ sample after FIB cutting. The average width and length of $MoSe_2$ are 4776.0 ± 51.6 nm and 5971.2 ± 5.6 nm, respectively. The nanomechanical device based on a spring-like "push-pull" mechanism (see the Supporting Information Section S5 for more details) was employed to investigate the in-plane tensile behavior of $MoSe_2$. The applied loading rate was 15 nm s^{-1} and the corresponding tensile strain rate was about 0.25% s^{-1}. All the tests were conducted in a SEM chamber through real-time observation, and the entire testing processes were recorded. The adhesion force between $MoSe_2$ and substrate was strong enough to firmly clamp the sample during tensile tests without marked slippage. Wrinkles in the ultrathin $MoSe_2$ samples were occasionally observed, due to their high flexibility. Figure 3b,e shows the SEM snapshots during a typical tensile test until fracture. The corresponding stress–strain curve is plotted in Figure 3f. Here the stress is calculated by $\sigma = F/(b \cdot h)$, where F is the measured

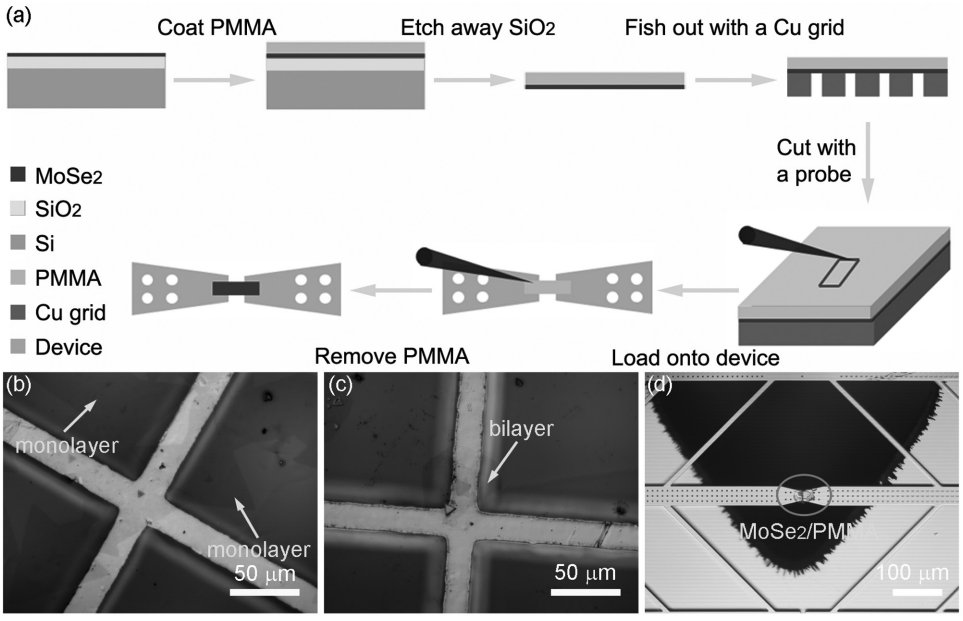

Figure 2. Schematic and optical images of $MoSe_2$ transfer. a) Schematic illustration of $MoSe_2$ transfer. b) Monolayer $MoSe_2$/PMMA sitting on a coper grid. c) Bilayer $MoSe_2$/PMMA sitting on a coper grid. d) $MoSe_2$/PMMA transferred onto a nanomechanical device.

in-plane force, b and h are respectively the initial width and thickness of the suspended $MoSe_2$ sample. The strain is calculated by $\varepsilon = \delta/a$, where δ is the elongation and a is the initial length of the $MoSe_2$ sample. Most tested samples were bilayer $MoSe_2$, whose thickness was measured as ≈1.4 nm by our AFM. This value is also in agreement with the bilayer thickness value in the literature.[23] As a tensile test began, the $MoSe_2$ sample was first straightened due to the existence of slack, as reflected by a flat toe region in the stress–strain curve. Once $MoSe_2$ was fully straightened, stress increased linearly with strain. The slope of the stress–strain curve gives the in-plane elastic modulus of $MoSe_2$. As the applied load reached a critical value, a major crack with the observable length of ≈200 nm appeared in $MoSe_2$, and this was followed immediately by fast propagation of the crack, resulting in catastrophic brittle fracture of the $MoSe_2$ sample (Figure 3e and associated video in the Supporting Information). The brittle fracture was also manifested as a sharp stress drop to zero (Figure 3f). Many $MoSe_2$ samples were used in our study. Unfortunately, most of them broke even during the transfer process, thus indicating a great challenge to the nanomechanical testing of fragile $MoSe_2$. A total of six tests were conducted successfully. The samples successfully tested did not contain any visible crack before testing. For bilayer $MoSe_2$, the interlayer van der Waals force seemed

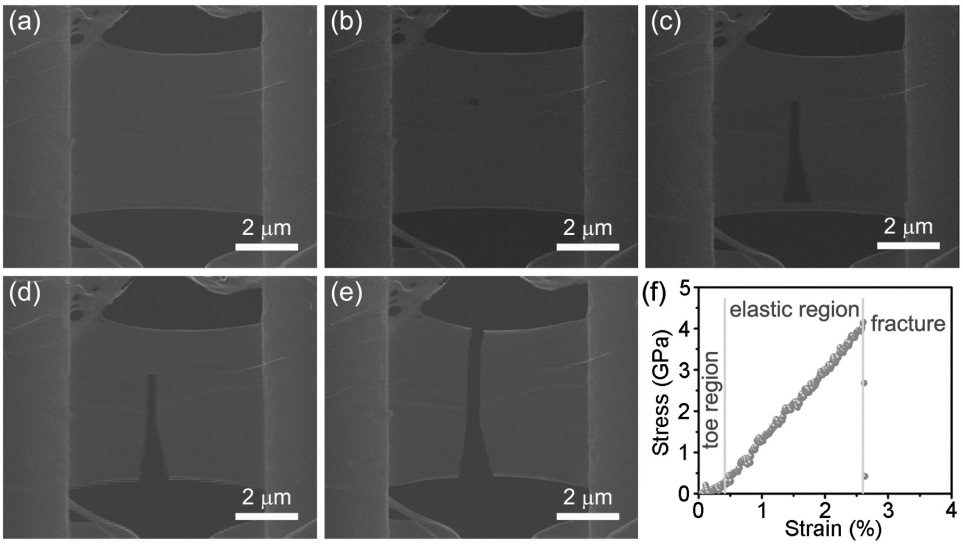

Figure 3. In situ tensile testing of a bilayer $MoSe_2$ sample. a) SEM image of $MoSe_2$ before tensile testing. b–e) SEM images showing the fracture process. f) Measured stress–strain curve; the associated results are listed in Table 1 (sample #4).

Table 1. Geometry and mechanical properties of suspended $MoSe_2$.

Sample #	Length [nm]	Width [nm]	Thickness [nm]	Critical load [μN]	Fracture strength [GPa]	Elastic modulus [GPa]
1	2885.2	8144.1	0.7	13.5	2.4	186.4
2	3803.0	4819.9	0.7	12.6	3.7	171.7
3	6107.3	6760.1	1.4	20.4	2.2	183.2
4	5971.2	4776.0	1.4	27.8	4.2	161.4
5	3023.2	7097.8	1.4	63.6	6.4	182.9
6	2666.7	16034.1	1.4	222.6	9.9	177.6
Average					4.8 ± 2.9	177.2 ± 9.3

to be strong enough to allow the top layer to deform together with the bottom layer. Therefore, the bilayer sample behaved like one piece. This was supported by our observation that no layer step was found around the fracture edges. **Table 1** lists the measured sample geometry, elastic modulus, critical fracture force, and fracture strength. The results are consistent between monolayer and bilayer $MoSe_2$. The average elastic modulus and fracture strength are 177.2 ± 9.3 and 4.8 ± 2.9 GPa, respectively. Note that we have excluded results from the tested $MoSe_2$ samples where pre-mature fracture initiated near the edge of the nanomechanical device, possibly due to the local non-uniformity of geometry and stress.

The elastic modulus from the above experimental measurement is consistent with the theoretical value of 162.1 GPa (**Table 2**) from our first principles density functional theory (DFT) calculations (see Method; the calculated thickness of monolayer $MoSe_2$ is 0.65 nm, in accordance with the DFT result in the literature[25]). However, the measured fracture strengths in Table 1 vary from 2.2 to 9.9 GPa, with a considerably large standard deviation of 2.9 GPa. To understand the origin of this large scattering, the morphology of our CVD-grown $MoSe_2$ was reexamined using optical microscope and AFM (Figure 1a,g; Supporting Information Section S6 shows an extreme case of large defects in CVD-grown $MoSe_2$, but the samples we tested did not contain any visible crack. However, flaws/cracks smaller than the detection limit of our instrument can pre-exist in as-grown samples, such that the apparent fracture strength of $MoSe_2$ can be reduced. Hence we reason that the variation of size of pre-existing flaws/cracks is responsible for the large scattering of measured fracture strengths. Recently, we have shown that the Griffith theory of brittle fracture is applicable to a 2D material of graphene by combining in situ fracture testing and atomistic modeling.[22] On this basis, we applied the Griffith theory to estimate the size of a dominant fracture-producing crack/flaw in the 2D $MoSe_2$ sample.[26] For a central crack of length $2a_0$, the Griffith theory of brittle fracture can be expressed as[27]

Table 2. DFT results of elastic constants of monolayer $MoSe_2$.

	C_{11} [GPa]	C_{12} [GPa]	Poisson's ratio	Elastic modulus [GPa]
$MoSe_2$	171.3	39.7	0.23	162.1

$$a_0 = \frac{2\gamma E}{\pi\sigma_c^2} \quad (1)$$

where E is the elastic modulus (Table 1) and γ is the surface energy which is defined as the edge energy of a 2D crystal divided by its thickness. It is difficult to directly measure the edge energy for a 2D crystal of $MoSe_2$ from experiment. Hence we performed DFT calculations (Experimental Section) to determine the theoretical value of γ. As shown in **Figure 4**, the $(10\bar{1}0)$ and $(11\bar{2}0)$ surfaces of monolayer $MoSe_2$ were modeled by a slab with two free edges along the $[10\bar{1}0]$ and $[11\bar{2}0]$ direction, respectively. The surface energy γ was calculated by the excess energy of the slab relative to the perfect monolayer divided by the nominal area of two free surfaces of the slab. We obtained the lowest surface energy of 1.55 J m^{-2} for the $(10\bar{1}0)$ surface (**Table 3**). This result is slightly lower than the corresponding DFT value of γ (1.68 J m^{-2}) for a bulk crystal of $MoSe_2$.[25] Then we used Equation (1) to estimate the length of the fracture-producing crack for all six samples tested. As shown in **Table 4**, the estimated crack lengths range from 3.6 to 77.5 nm, with an average value of 33.0 ± 30.9 nm.

The above estimate of crack lengths in the range of tens of nanometers implies that the fracture properties of an ultrathin 2D material such as $MoSe_2$ depend heavily on the quality of the individual single crystal through, for example, the largest pre-existing flaw. It follows that samples with smaller flaws should possess higher apparent fracture strengths. In our simple estimation, only the "weakest link"[27] – a dominant fracture-producing crack – is considered. However, there might exist more pre-existing flaws with different sizes and spatial distributions in a 2D sample. These flaws could interact with each other under an applied load and collectively lead to fracture. In this scenario, resolving the controlling fracture mechanism requires a more detailed experimental characterization of the statistics and evolution of flaws during testing, which is a necessary step for understanding the fracture strength of brittle 2D materials governed by the extreme value statistics of defects.[27] We also note that while the present study underscores the effect of pre-existing flaws on the apparent fracture strength of 2D single crystals, grain boundaries in the case of 2D polycrystals (e.g., a typical polycrystalline graphene) are expected to have a statistical distribution of breaking strengths and thus can play an important role in governing the apparent fracture strength of 2D polycrystals.[28]

It is interesting to compare the brittleness between graphene and $MoSe_2$. The present nanomechanical testing has revealed the brittle fracture of large-area single crystals of $MoSe_2$. But we are not able to quantitatively measure the fracture toughness of $MoSe_2$, which is an important mechanical property that describes the ability of a material containing a crack to resist fracture. Measurement of fracture toughness requires a finite-sized pre-crack in the sample. When we attempted to cut a pre-crack in $MoSe_2$ through FIB, catastrophic fracture was unavoidable during the cutting process, suggesting the brittleness of $MoSe_2$. The SEM images of monolayer $MoSe_2$ with multiple cracks induced during FIB cutting can be found in the Supporting Information Section 7. Such a fragile behavior can be correlated to the aforementioned difficulty of dry transfer of $MoSe_2$ samples that were easily breakable during transfer.

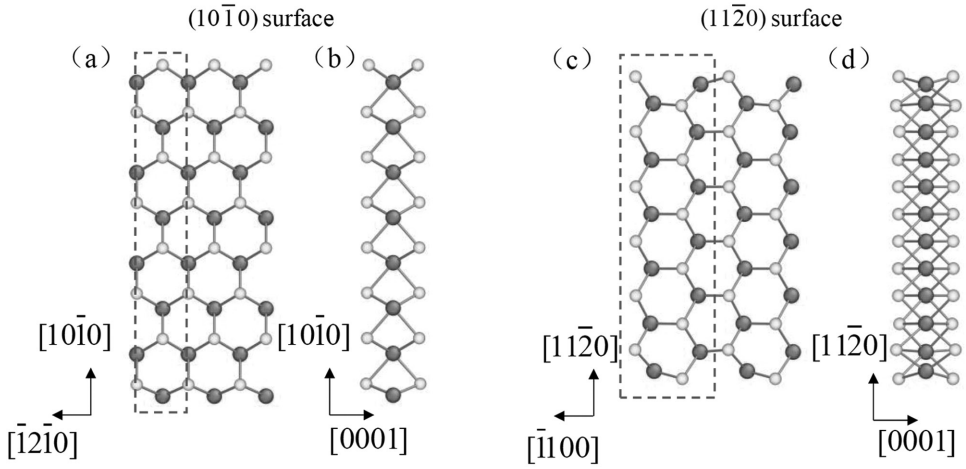

Figure 4. Atomic structure of monolayer $MoSe_2$ slabs after DFT relaxation. a) Basal-plane view and b) cross-sectional view of a $MoSe_2$ slab with (10$\bar{1}$0) free surfaces. c) Basal-plane view and d) cross-sectional view of a $MoSe_2$ slab with (11$\bar{2}$0) free surfaces. Due to lattice periodicity in the basal plane, only the region highlighted by the rectangle is adopted in DFT calculations.

Previously, the brittle fracture of fast crack growth in graphene has been observed.[22,29] However, in contrast to the fragile $MoSe_2$, we were able to introduce a pre-crack in graphene by FIB cutting and further quantitatively measured its fracture toughness. Such contrast indicates that $MoSe_2$ is more brittle than graphene. To rationalize this difference, we note that for brittle materials, the fracture toughness is approximately twice the surface energy. From DFT calculations, the lowest surface energy in the basal plane of $MoSe_2$ and graphene are ≈1.55 and 4.76 J m^{-2} (Table 3), respectively. The corresponding theoretical value of fracture toughness is respectively 3.1 and 9.5 J m^{-2}, the latter of which is consistent with an experimental value of 15.9 J m^{-2},[22] given the fact that loading orientations and polycrystalline structures could influence the experimental results. The fairly large difference in fracture toughness between graphene and $MoSe_2$ thus explains why $MoSe_2$ is more brittle than graphene. Table 3 also lists the DFT result of the lowest surface energy of 1.83 J m^{-2} for another 2D TMD material of MoS_2, which is only slightly larger than that of $MoSe_2$. This suggests that MoS_2 is more brittle than graphene as well. In the future, it would be interesting to further explore quantitative measurement of the fracture toughness of $MoSe_2$ and MoS_2, for comparison with that of graphene.

Table 3. Comparison of DFT results of surface energy and edge energy between monolayer $MoSe_2$, MoS_2, and graphene for the (10$\bar{1}$0) (zigzag) and (11$\bar{2}$0) (armchair) edges.

Monolayer	Thickness [nm]	Orientation	Edge energy [eV Å^{-1}]	Surface energy [γ] [J m^{-2}]
$MoSe_2$	0.65	zigzag	0.63	1.55
		armchair	0.65	1.60
MoS_2	0.619	zigzag	0.71	1.83
		armchair	0.72	1.87
Graphene	0.331	zigzag	1.30	6.26
		armchair	0.98	4.76

In summary, we have developed an in situ nanomechanical testing platform for quantitative measurement of the mechanical proprieties of 2D materials inside SEM. In contrast to the local, transverse probing by AFM, our device enables a uniform in-plane loading of the freestanding 2D sample. Our testing is facilitated by a new technique of dry transfer of the ultrathin 2D sample to the loading device. We perform in situ tensile tests of monolayer and bilayer $MoSe_2$, and observed the brittle fracture processes of crack initiation, propagation, and final failure in real time. The measured elastic modulus and fracture strength of $MoSe_2$ are 177.2 ± 9.3 and 4.8 ± 2.9 GPa, respectively. The large variation of fracture strengths is attributed to the pre-existing flaws caused by CVD growth. Based on the Griffith theory of fracture, we estimate the fracture-producing crack size as 33.0 ± 30.9 nm. Finally, we discuss implications of our results on the statistical strength as well as the fragility of brittle 2D materials.

Experimental Section

Growth of $MoSe_2$: Molybdenum trioxide (MoO_3) powder and selenium (Se) powder were selected as precursors to grow $MoSe_2$ on a clean Si/SiO_2 (275 nm thick) wafer in a tube furnace (Lindbergh/Blue M, Thermo Scientific). The growth temperature was controlled at 750 °C.

Table 4. Pre-existing crack length of $2a_0$ calculated by the Griffith theory.

Sample #	Fracture strength [GPa]	Elastic modulus [GPa]	Surface energy [γ] [J m^{-2}]	$2a_0$ [nm]
1	2.2	183.2	1.55	77.5
2	2.4	186.4	1.55	65.3
3	3.7	171.7	1.55	24.3
4	4.2	161.4	1.55	18.5
5	6.4	182.9	1.55	8.8
6	9.9	177.6	1.55	3.6
Average	4.8 ± 2.9	177.2 ± 9.3		33.0 ± 30.9

The Se powder was loaded upstream at 200 °C to slowly generate the Se vapor. A mixture of argon and hydrogen (10 vol% hydrogen) with a total flow rate of 200 sccm served as a carrier gas. The number of $MoSe_2$ layers was first differentiated by the color of $MoSe_2$ and confirmed by the thickness measured with an AFM (Agilent PicoScan 5500). The microstructures and morphologies were also characterized by a suite of characterization tools, including optical microscope (The Micromanipulator Co., Inc.), scanning electron microscope (SEM, FEI Quanta 400), transmission electron microscope (TEM, JEOL 2100 F) with an accelerating voltage of 200 kV, and Raman spectroscopy (Renishaw inVia).

Dry Transfer: A "dry transfer" technique was used to transfer an ultrathin $MoSe_2$ membrane onto the nanomechanical device for in situ tensile testing. To this end, a thin layer of PMMA with thickness of 200–300 nm was first coated over $MoSe_2$ grown on a Si/SiO_2 wafer. They were then heated to 180 °C and held for 1 min using a hot plate to make good contact between $MoSe_2$ and PMMA. The Si/SiO_2 wafer was slowly dropped into NaOH solution with the concentration of 2.5 mol L^{-1}. After 2 h, the SiO_2 was etched away and the PMMA/$MoSe_2$ floated on the NaOH solution. Another piece of clean Si wafer was used to fish out PMMA/$MoSe_2$ and slowly immerged into water to wash away residual NaOH. Finally, the PMMA/$MoSe_2$ was fished out by a copper grid. The monolayer and bilayer $MoSe_2$ was observable with optical microscope. A fine tungsten probe installed in a micromanipulator was employed to cut a piece of PMMA/$MoSe_2$ out of the film. The PMMA/$MoSe_2$ was picked up by the same W probe and gently loaded onto the nanomechanical device. To obtain the freestanding $MoSe_2$, the whole device together with PMMA/$MoSe_2$ was put in a tube furnace (Lindbergh/Blue M, Thermo Scientific) under continuous flow of a mixture of 90% N_2 and 10% H_2 at 200 sccm to paralyze PMMA. The temperature was raised to 350 °C at a ramping rate of 10 °C min^{-1} and held at 350 °C for 1 h followed by natural cooling down to room temperature.

Mechanical Testing: After the above paralysis step, the monolayer $MoSe_2$ sample was cut by FIB in a SEM (FEI, Helios 660). To avoid cutting damages, a minimum beam current of 1 pA was used to cut a corner-rounded rectangular sample. The sample-loaded microdevice was subsequently glued to an SEM sample stub using crystal bond. The microdevice operates based on a spring-like "push-pull" mechanism. Details about nanomechanical device can be found in the Supporting Information Section S5. A quantitative Agilent nanoindenter was used to actuate the device and also to measure the load and displacement independently. The tensile testing was monitored through SEM for ensuring the validity of tests as well as visualizing the deformation and fracture processes.

First Principles Calculations: Our first-principles calculations are based on electronic DFT and carried out with the VASP code.[30] The ion-electron interaction is represented by the projector augmented wave method[31] and the exchange-correction functional is described within the generalized gradient approximation in the parametrization of Perdew–Burke–Ernzerhof.[32] The plane wave cutoff energy was 400 eV. As shown in Figure 4, the $(10\bar{1}0)$ and $(11\bar{2}0)$ surfaces of monolayer $MoSe_2$ were modeled by a slab with two free edges in the $[10\bar{1}0]$ and $[11\bar{2}0]$ direction in the basal plane, respectively. The surface energy of monolayer $MoSe_2$ was defined as $\gamma=(E_{slab}-E_{monolayer})/A$, where E_{slab} is the total energy of the slab, $E_{monolayer}$ is the total energy of the perfect monolayer with the same number of atoms as the slab, and A is the surface area. The specific slab models for the $(10\bar{1}0)$ and $(11\bar{2}0)$ surface used in our first principles calculations contain 24 and 36 atoms in the supercell, respectively, as indicated by the dashed line in Figure 4. In this supercell setup with periodic boundary conditions, slabs in two neighboring supercells were separated from each other by a 20 Å thick vacuum space in the direction of free surface. A large spacing of 20 Å in the [0001] direction was used to prevent interactions between 2D monolayers. The number of layers and the thickness of vacuum space have been tested to be converged. A $13\times1\times1$ and $9\times1\times1$ k-points mesh was adopted for the slab models of $(10\bar{1}0)$ and $(11\bar{2}0)$ surface (Figure 4) according to the Monkhorst-Pack scheme,[33] respectively. The energy convergence of the electronic self-consistency is on the order of 10^{-6} eV. The relaxation is converged when the maximum force on each atom is less than 0.01 eV $Å^{-1}$. In addition, we calculated the thickness of monolayer $MoSe_2$ by using a bulk $MoSe_2$ crystal with the optB86b-vdW functional,[34] which is accurate for characterizing the van der Waals interaction between $MoSe_2$ interlayers.[25] The above DFT schemes are also used to calculate the edge energy and surface energy for monolayer graphene and MoS_2. The obtained DFT results for graphene are identical to those reported in the literature,[35] thus validating our DFT schemes.

Supporting Information

Supporting Information is available from the Wiley Online Library or from the author.

Acknowledgements

Y.Y. and X.L. contributed equally to this work. Y.Y. and J.L. acknowledge support from the Air Force Office of Scientific Research BRI Grant FA9550-14-1-0628, the Welch Foundation Grant C-1716, and the Department of Energy, Office of Basic Energy Sciences under contract DE-FG02-13ER46967. T.Z. acknowledges funding from NSF grant DMR-1410331. X.L., Q.C., and J.L. thank support from NSF of China (Grant No. 11528407). DFT simulations were performed on the "Explorer 100" cluster system of Tsinghua National Laboratory for Information Science and Technology, Beijing, China.

Note: The Acknowledgements were updated on January 4, 2017, after initial publication online. The caption of Figure 1 and the text on page 1 and 2 were also updated to reflect that the figure is presented in grayscale.

Received: August 5, 2016
Revised: September 22, 2016
Published online: November 3, 2016

[1] Y. M. Shi, H. N. Li, L. J. Li, *Chem. Soc. Rev.* **2015**, *44*, 2744.
[2] Y. R. Lim, W. Song, J. K. Han, Y. B. Lee, S. J. Kim, S. Myung, S. S. Lee, K. S. An, C. J. Choi, J. Lim, *Adv. Mater.* **2016**, *28*, 5025.
[3] S. Tongay, J. Zhou, C. Ataca, K. Lo, T. S. Matthews, J. B. Li, J. C. Grossman, J. Q. Wu, *Nano Lett.* **2012**, *12*, 5576.
[4] W. Z. Wu, L. Wang, Y. L. Li, F. Zhang, L. Lin, S. M. Niu, D. Chenet, X. Zhang, Y. F. Hao, T. F. Heinz, J. Hone, Z. L. Wang, *Nature* **2014**, *514*, 470.
[5] X. L. Wang, Y. J. Gong, G. Shi, W. L. Chow, K. Keyshar, G. L. Ye, R. Vajtai, J. Lou, Z. Liu, E. Ringe, B. K. Tay, P. M. Ajayan, *ACS Nano* **2014**, *8*, 5125.
[6] B. Radisavljevic, A. Radenovic, J. Brivio, V. Giacometti, A. Kis, *Nat. Nanotechnol.* **2011**, *6*, 147.
[7] S. Das, H. Y. Chen, A. V. Penumatcha, J. Appenzeller, *Nano Lett.* **2013**, *13*, 100.
[8] U. Bhanu, M. R. Islam, L. Tetard, S. I. Khondaker, *Sci. Rep.* **2014**, *4*, 5575.
[9] C. H. Lee, G. H. Lee, A. M. van der Zande, W. C. Chen, Y. L. Li, M. Y. Han, X. Cui, G. Arefe, C. Nuckolls, T. F. Heinz, J. Guo, J. Hone, P. Kim, *Nat. Nanotechnol.* **2014**, *9*, 676.
[10] B. Amin, N. Singh, U. Schwingenschlogl, *Phys. Rev. B* **2015**, *92*, 075439.
[11] O. Lopez-Sanchez, D. Lembke, M. Kayci, A. Radenovic, A. Kis, *Nat. Nanotechnol.* **2013**, *8*, 497.
[12] Y. Zhang, Y. Q. Yu, L. F. Mi, H. Wang, Z. F. Zhu, Q. Y. Wu, Y. G. Zhang, Y. Jiang, *Small* **2016**, *12*, 1062.
[13] M. Chhowalla, H. S. Shin, G. Eda, L. J. Li, K. P. Loh, H. Zhang, *Nat. Chem.* **2013**, *5*, 263.
[14] J. J. Wu, M. J. Liu, K. Chatterjee, K. P. Hackenberg, J. F. Shen, X. L. Zou, Y. Yan, J. Gu, Y. C. Yang, J. Lou, P. M. Ajayan, *Adv. Mater. Interfaces* **2016**, *3*, 1500669.

[15] Q. P. Lu, Y. F. Yu, Q. L. Ma, B. Chen, H. Zhang, *Adv. Mater.* **2016**, *28*, 1917.
[16] C. Lee, X. D. Wei, J. W. Kysar, J. Hone, *Science* **2008**, *321*, 385.
[17] J. W. Suk, R. D. Piner, J. H. An, R. S. Ruoff, *ACS Nano* **2010**, *4*, 6557.
[18] O. V. Yazyev, Y. P. Chen, *Nat. Nanotechnol.* **2014**, *9*, 755.
[19] A. Castellanos-Gomez, M. Poot, G. A. Steele, H. S. J. van der Zant, N. Agrait, G. Rubio-Bollinger, *Adv. Mater.* **2012**, *24*, 772.
[20] L. Song, L. J. Ci, H. Lu, P. B. Sorokin, C. H. Jin, J. Ni, A. G. Kvashnin, D. G. Kvashnin, J. Lou, B. I. Yakobson, P. M. Ajayan, *Nano Lett.* **2010**, *10*, 3209.
[21] S. Bertolazzi, J. Brivio, A. Kis, *ACS Nano* **2011**, *5*, 9703.
[22] P. Zhang, L. L. Ma, F. F. Fan, Z. Zeng, C. Peng, P. E. Loya, Z. Liu, Y. J. Gong, J. N. Zhang, X. X. Zhang, P. M. Ajayan, T. Zhu, J. Lou, *Nat. Commun.* **2014**, *5*, 3782.
[23] J. Xia, X. Huang, L. Z. Liu, M. Wang, L. Wang, B. Huang, D. D. Zhu, J. J. Li, C. Z. Gu, X. M. Meng, *Nanoscale* **2014**, *6*, 8949.
[24] S. Horzum, H. Sahin, S. Cahangirov, P. Cudazzo, A. Rubio, T. Serin, F. M. Peeters, *Phys. Rev. B* **2013**, *87*, 125415.
[25] H. Mirhosseini, G. Roma, J. Kiss, C. Felser, *Phys. Rev. B* **2014**, *89*, 205301.
[26] T. Zhu, J. Li, *Prog. Mater. Sci.* **2010**, *55*, 710.
[27] B. Lawn, *Fracture of Brittle Solids*, Cambridge University Press, Cambridge, UK **1993**.
[28] A. Shekhawat, R. O. Ritchie, *Nat. Commun.* **2016**, *7*, 10546.
[29] X. L. Wei, S. Xiao, F. X. Li, D. M. Tang, Q. Chen, Y. Bando, D. Golberg, *Nano Lett.* **2015**, *15*, 689.
[30] G. Kresse, J. Furthmuller, *Phys. Rev. B* **1996**, *54*, 11169.
[31] G. Kresse, D. Joubert, *Phys. Rev. B* **1999**, *59*, 1758.
[32] J. P. Perdew, K. Burke, M. Ernzerhof, *Phys. Rev. Lett.* **1996**, *77*, 3865.
[33] H. J. Monkhorst, J. D. Pack, *Phys. Rev. B* **1976**, *13*, 5188.
[34] J. Klimes, D. R. Bowler, A. Michaelides, *Phys. Rev. B* **2011**, *83*, 195131.
[35] P. Koskinen, S. Malola, H. Hakkinen, *Phys. Rev. Lett.* **2008**, *101*, 115502.